

An Intelligent Vision Mobile Measurement Approach for High-speed Inspection of Large-size Flatness

Dongwei Qiu,¹ Mingjian Xiao,¹ Shanshan Wan,^{2*} and Xingyu Wang¹

¹School of Geomatics and Urban Spatial Informatics,
Beijing University of Civil Engineering and Architecture, Beijing 100044, P.R. China

²School of Electrical and Information Engineering,
Beijing University of Civil Engineering and Architecture, Beijing 100044, P.R. China

(Received January 13, 2022; accepted April 20, 2022; online published May 11, 2022)

Keywords: large-size surface detection, intelligent vision mobile platform, binocular vision, flatness detection, satellite antenna

In current science and engineering, the demand for large-size surface detection has increased considerably. However, large-size surface detection presents some challenges, such as very large detection target area, discontinuous detection surface, and low detection accuracy. The current detection methods are mainly based on in-position detection and cannot meet the requirements of detection speed and accuracy for large-size surface detection. In this paper, we propose a fast detection method for large-scale flatness based on an intelligent vision mobile platform (IVMP). Specifically, by establishing the path optimization model, beam adjustment model, and large-scale flatness calculation model for the IVMP, the binocular vision acquisition of large-scale target information and fast large-scale shape detection are realized. The rigidly fixed position relation of binocular vision is considered, and the parameters of the main camera can be obtained through an error equation, then the parameters of the assistant camera can be acquired quickly to calculate the three-dimensional coordinates of space points. The particle swarm optimization algorithm is integrated into the differential evolution algorithm to improve the detection speed. The IVMP is applied to the flatness detection of a satellite antenna. The experimental results show that the detection precision and efficiency of the IVMP are clearly higher than those of the laser tracking and theodolite systems.

1. Introduction

With the rapid development of the manufacturing industry, precision industries have adopted increasingly stringent requirements.⁽¹⁾ Flatness inspection is one of the most important tasks in precision machining, and many industries use flatness as a reference standard.^(2,3) For instance, the shape error of the antenna surface during the manufacturing of large-size satellite antennas affects the performance of the satellite, and it is necessary to ensure that the flatness meets the design standard.⁽⁴⁾

*Corresponding author: e-mail: wss@bucea.edu.cn
<https://doi.org/10.18494/SAM3854>

Various methods have been proposed to realize flatness detection. Li *et al.*⁽⁵⁾ proposed a method of accurately detecting the flatness of large plates, in which two laser trackers were arranged at two specific locations, and the coordinates of the same target point were used to calculate the flatness. Zhu *et al.*⁽⁶⁾ proposed a laser tracking detection method based on station movement measurements. The flatness detection method depends on a laser tracker, and it has the advantages of high precision, high efficiency, and large detection range, and the method can realize mobile in-position detection. However, its implementation requires contact detection, skilled operators, and expensive equipment. Li⁽⁷⁾ proposed a flatness detection method using a digital display micrometer array to place a workpiece on a pallet correctly. A dial indicator array is in contact with the surface of the workpiece to obtain shape information point by point. The method can be used to automatically and quickly perform flatness detection, and it is inexpensive and convenient to use. However, this method is only suitable for the flatness detection of small workpieces, and the instrument is relatively sensitive to vibrations, so the mechanical base must be damped with appropriate spacers. Chen *et al.*⁽⁸⁾ proposed a high-precision micro-scale flatness measuring machine composed of a multi-beam angle sensor (MBAS). A micro-scale flatness measuring machine is used to detect the flatness of a workpiece by rotating the workpiece around a fixed radius circle. This method uses only one MBAS probe to achieve precise flatness measurement. It can eliminate the homodyne error of circumferential scanning and automatically eliminate the tilt error caused by the rotation of the workpiece when the angle is detected. However, this method is only suitable for detecting the flatness of small workpieces, its detection efficiency is low, and it is difficult to meet the need for rapid detection. Fujimoto *et al.*^(9,10) proposed a three-point method with an autonomous calibration function to detect the flatness of a target. This method uses three built-in displacement sensors to measure the flatness of the target. This approach can automatically reduce the effects of the motion error and zero-point difference of the three displacement sensors built into the wafer holder. However, the studies only illustrate the conceptual design of this method by introducing theoretical analysis and numerical calculation.

The above detection methods are widely used in different detection fields, detection environments, and detection objects because of their respective advantages in detection accuracy, detection range, portability, and applicability. However, in the detection of large-size, discontinuous surfaces and folded antennas, the existing detection methods are not well suited. They require a long detection time and are limited because of their low efficiency and speed. Moreover, they cannot achieve mobile in-position detection. Furthermore, these approaches cannot achieve discontinuous surface detection and cannot provide large-scale flatness autonomous rapid detection. Hence, it is necessary to develop a new detection approach that can realize high-precision, high-efficiency, autonomous, and rapid flatness detection, especially for large-size and discontinuous surfaces.

Visual inspection technology has the potential to meet the needs of large-size and discontinuous surfaces and autonomous rapid flatness detection owing to its advantages such as flexibility, mobility, automation, noncontact, and portability. We propose an intelligent vision mobile platform (IVMP) for the automatic and high-speed detection of large-size flatness. The platform is mainly integrated with an automated guided vehicle (AGV), binocular vision, a

computer control system, lifting slides, and a rotating platform. On the basis of the path planning and flatness calculation models, this approach can accurately, autonomously, and rapidly detect large-scale flatness. Through experimental comparison and accuracy analysis, the detection accuracy of the IVMP for large-size flatness is higher than 5×10^{-2} mm, compared with those of the API tracker 3 laser tracking system⁽¹¹⁾ and Leica theodolite system.⁽¹²⁾ The flatness detection accuracy of the theodolite system is 10% higher. The comparison of the IVMP with the laser tracking and theodolite systems showed that the detection efficiency of the IVMP is 48 and 60.6% higher, respectively. In addition, the approach can realize mobile in-position detection, discontinuous surface detection, and autonomous rapid detection, and has strong robustness, reliability, and accuracy, which can meet the needs of large-scale, discontinuous surface flatness detection.

2. IVMP

To better introduce the fast detection method of large-scale flatness, we first give the detection platform, IVMP, that is designed according to the method proposed in this paper; hence, an intuitive cognition of the method can be established.

In this section, a new type of intelligent, autonomous, and rapid precision inspection platform developed on the basis of visual technology is presented. Figure 1 shows a schematic representation of the IVMP for the autonomous and rapid detection of large-size flatness. The height of the IVMP is at least 2.5 m. During flatness inspection, the height of the rotating platform is adjusted within the range of 0.45–2.5 m on the lifting slide. The work of the IVMP is controlled by a computer control system and dedicated data processing software, without any user intervention. The IVMP is designed and developed according to the characteristics of the

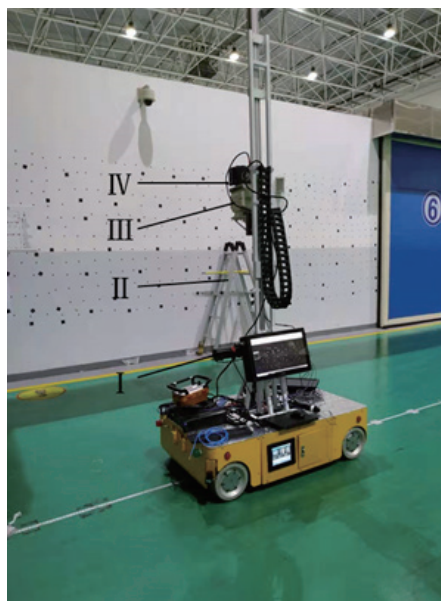


Fig. 1. (Color online) IVMP

antenna and the needs for its monitoring. The system was first tested in laboratory settings and, after multiple iterations and improvements, the IVMP was finally deployed in the detection field.

The IVMP shown in Fig. 1 includes an automated guided vehicle (AGV), a lifting slide, a rotating platform, binocular vision, a data line, a computer control system, and special data processing software installed in the computer. The AGV is a transportation vehicle that uses a battery as a power source, can rely on various sensors to obtain external information, and can automatically follow a planned path. Under the supervision of the computer control system, the AGV automatically follows the planned path according to the instructions issued by the computer, avoids obstacles, and accurately stops at the task location to complete the work. The platform has two postures: horizontal rotation and vertical rotation. The AGV moves following the established path planning model.

The computer control system is shown in Fig. 1(I). The power of the computer control system is 200 W, and the AGV provides 24 V power. A data processing system is installed on the computer, which can control the AGV, lifting slide, rotating platform, and binocular vision in real time. It can realize the automatic image recognition, automatic matching, automatic splicing, automatic adjustment calculation of three-dimensional coordinate data, and flatness calculation.

The datum ruler provides the length datum in the adjustment calculation. Since satellite antenna flatness detection requires a highly stable length reference, we use an indium steel reference ruler in this study [Fig. 1(II)], which can provide a high-precision and stable length reference for the IVMP.

Figure 1(III) is a three-degree-of-freedom automatic rotating platform. The rotating platform can continuously and automatically rotate to a predetermined angle around three axes. The rotation angle accuracy is not more than 0.5° . The rotation speed should be in the range of 0.05–30%/s. The rotating platform will move up and down according to computer instructions.

Binocular vision is shown in Fig. 1(IV). The image information of the antenna surface is collected and transmitted to the computer. The technical parameters of binocular vision are shown in Table 1.

The computer needs to control the binocular vision, rotating platform, slide rail, and AGV for communication integration and interaction (Fig. 2). The AGV supplies power to the computer. The computer supplies power to binocular vision and the lifting platform. Data processing software supports binocular vision for fast, real-time, and dynamic detection. According to the path planning model, the flatness of large-scale and discontinuous antennas can be detected automatically and quickly. The high-precision splicing, real-time display, and feedback of detection results can also be realized.

The AGV is activated after the communication integration interaction. Following the path planning model, the starting point command is sent at the starting point. A trigger command is

Table 1
Technical parameters of binocular camera.

Resolution	Pixel	Pixel size	Focal length	Field angle
6576 × 4384	29 million	5.5 mm × 5.5 mm	24 mm	72° × 51

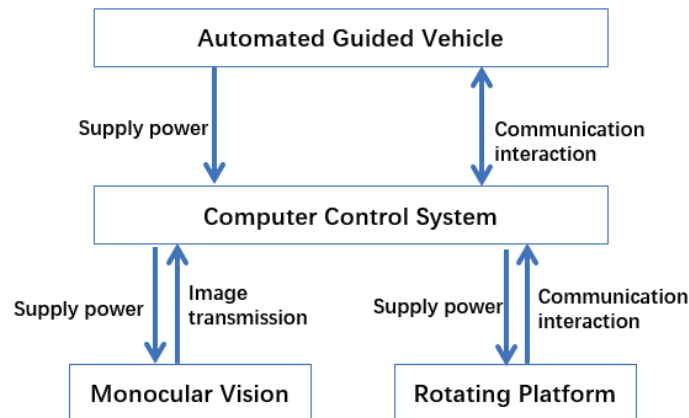


Fig. 2. (Color online) Schematic diagram of communication integration interaction of IVMP.

sent each time when the monitoring station is reached, then the binocular vision performs data collection. When the platform reaches the endpoint position, an endpoint signal is sent, and when the AGV stops moving, the binocular vision stops data collection as well. The computer control system transmits and displays the image information in real time through a serial port data line. After the detection is completed, the data processing software performs matching, splicing, and adjustments automatically to calculate quickly the coordinates of the landmark points and the flatness of the antenna.

3. Fast Detection Approach Based on IVMP

The approach of flatness detection mainly includes three steps, which are shown in Fig. 3.

- Step 1. Establish an IVMP path planning model. Without manual intervention, the platform can achieve autonomous rapid image information acquisition according to the path planning model.
- Step 2. Establish a beam adjustment model, then the IVMP can realize the automatic identification, automatic positioning, automatic acquisition, real-time transmission, automatic matching and processing, and high-precision calculation of the three-dimensional coordinates of large-size antenna landmark points.
- Step 3. Establish a large-size antenna flatness calculation model to realize the autonomous rapid calculation and feedback of large-size antenna flatness.

3.1 Path planning model

In the process of flatness detection, the detection of the net shape and the detection of the intersection angle are important parts of the visual inspection. The optical axis of binocular vision should maintain an angle of 45° with the antenna surface normal. Binocular vision adopts a level detection attitude (Fig. 4) and a vertical detection attitude (Fig. 5) for continuous image information acquisition. The first takes pictures in a horizontal posture, then rotates 90° along

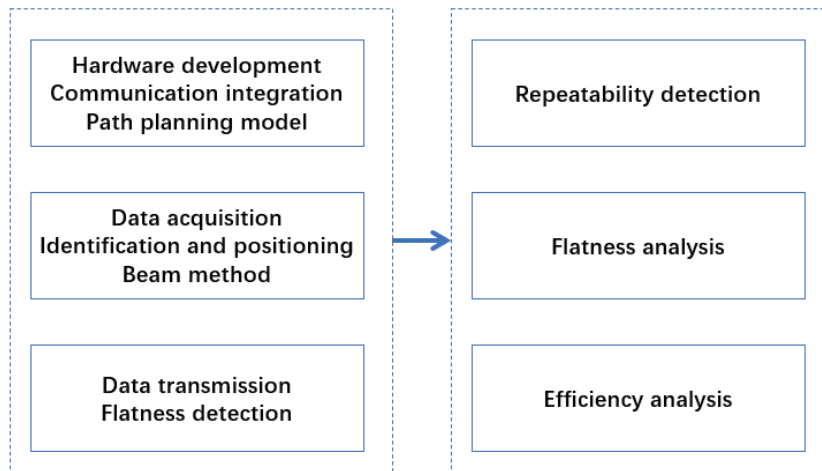


Fig. 3. (Color online) Flatness detection roadmap of IVMP.

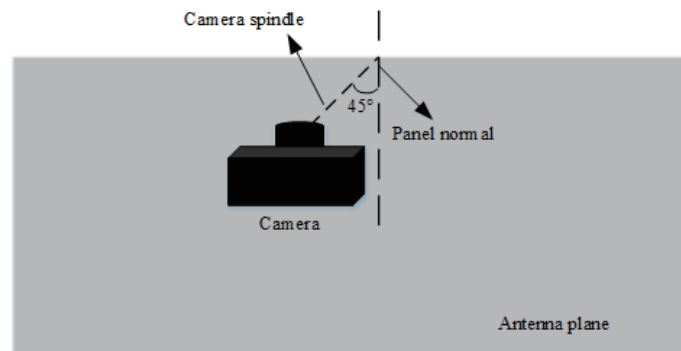


Fig. 4. Binocular vision for level detection attitude.

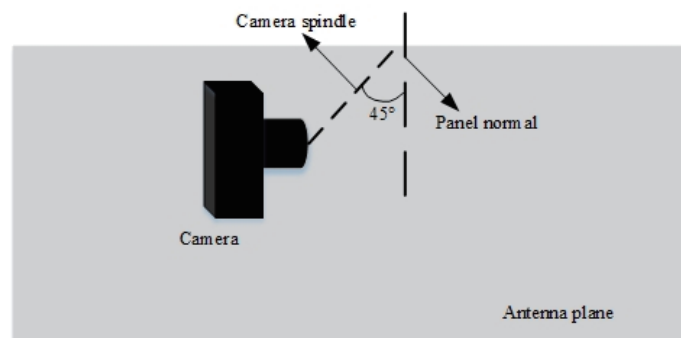


Fig. 5. Binocular vision for vertical detection attitude.

the main axis, and the light axis of binocular vision still maintains an angle of 45° relative to the normal of the panel, and then the vertical posture detection of the antenna surface is performed.

Assume that the target plane is perpendicular to the optical axis of the camera, as shown in Fig. 6. To capture a complete target plane image at a fixed height for binocular vision, the closest distance between binocular vision and the target plane must be determined. On the basis of the

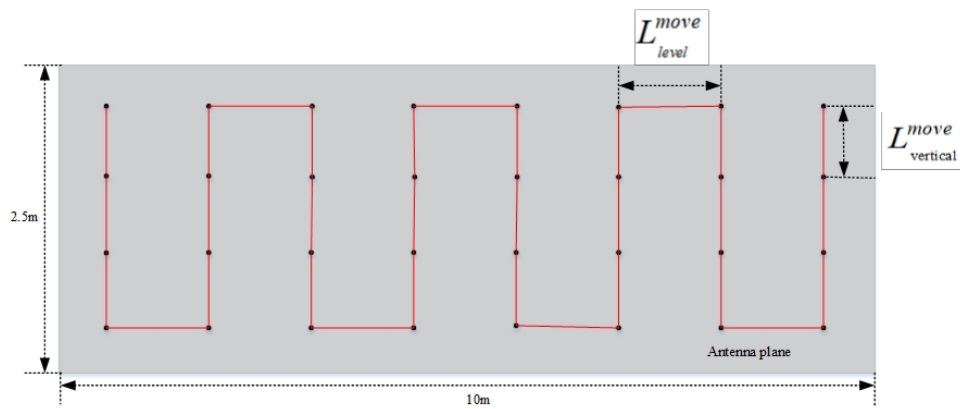


Fig. 7. (Color online) Image acquisition path.

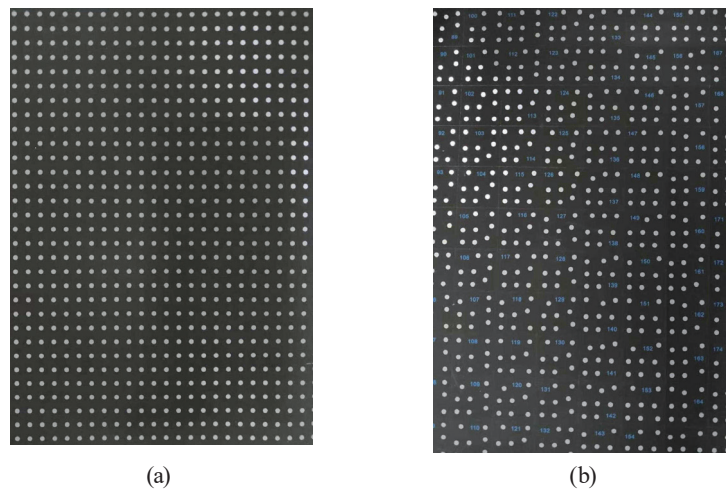


Fig. 8. (Color online) Design of landmark points: (a) calibration and (b) coding points.

recognition and location algorithm based on the edge is adopted. On the basis of the automatic identification of landmarks, automatic positioning, automatic matching, and independent rapid processing are further realized.⁽¹⁵⁾

In Fig. 8, the landmark points are made of a directional reflective material referred to as the retro-reflective target (RRT). The images of landmark points show “quasi binary images”.

After the landmark points are projected into an ellipse image, it is necessary to extract the ellipse edge that meets certain requirements. The image processed by the Canny operator contains a false or non-landmark edge. It is necessary to detect the edge and the pixels defining the edge to identify the landmark.⁽¹⁶⁾

The IVMP in the state of motion detection, using high-resolution binocular vision for the large size of the antenna layout landmark film surface, obtains a quasi-binary digital image on the surface of the antenna through computer digital image processing, image matching, triangulation, and adjustment calculation and a series of accurate three-dimensional coordinate landmarks after processing.

To detect the accuracy of the flatness of satellite antennas, the approach adopts binocular vision for image shooting. When the satellite antenna plane is photographed by binocular vision, the first binocular vision calibration is carried out by using Zhang Zhengyou calibration methods,⁽¹⁷⁾ and the initial values of internal and external parameters of binocular vision are obtained. The strategy of the approach is that the IVMP is equipped with binocular vision, and the two cameras are rigidly fixed and integrated into a whole to achieve satellite antenna image acquisition, as shown in Fig. 9. One of the cameras is taken as the main camera, and the external parameters of the main camera are taken as the parameters to be optimized by the beam adjustment method. The other camera is used as the assistant camera, so the external parameters of the assistant camera are represented by the external parameters of the main camera.

On the basis of binocular vision, assume one main camera and one assistant camera. According to the beam adjustment method, the imaging model of the main camera can be obtained, as shown in Eq. (3).

$$\lambda \begin{bmatrix} u_{main} \\ v_{main} \end{bmatrix} = K_{main} \begin{bmatrix} R_{main} & T_{main} \end{bmatrix} \begin{bmatrix} X \\ Y \\ Z \\ 1 \end{bmatrix} \tag{3}$$

Here, (u_{main}, v_{main}) represents pixel coordinates of pictures taken by the main camera, K_{main} represents internal parameters of the main camera, (R_{main}, T_{main}) represents external parameters of the main camera, and (X, Y, Z) represents world coordinates of three-dimensional points.

The error equation of the main camera is obtained on the basis of the imaging model, as shown in Eq. (4).

$$V_{main} = \begin{bmatrix} M_{main} & N_{main} \end{bmatrix} \begin{bmatrix} \delta_{cmain} \\ \delta_{tmain} \end{bmatrix} - L_{main} \tag{4}$$

Here, (M_{main}, N_{main}) represents the first-order partial derivative of the external parameters of the

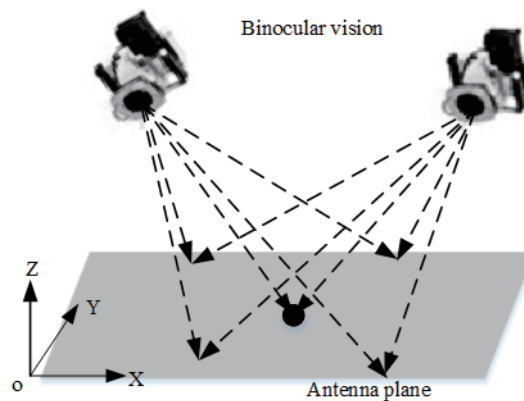


Fig. 9. Principle of binocular visual detection.

main camera and three-dimensional points; $(\delta_{cmain}, \delta_{tmain})$ represents the correction of the external parameters of the main camera and the correction of three-dimensional points; L_{main} represents the difference matrix between the actual coordinates of image points and the reprojection coordinates calculated with the imaging model, as shown in Eq. (5).

$$\left\{ \begin{array}{l} M_{main} = \begin{bmatrix} \frac{\partial u_{main}}{\partial \omega_{main}} & \frac{\partial u_{main}}{\partial \varphi_{main}} & \frac{\partial u_{main}}{\partial \kappa_{main}} & \frac{\partial u_{main}}{\partial t_{xmain}} & \frac{\partial u_{main}}{\partial t_{ymain}} & \frac{\partial u_{main}}{\partial t_{zmain}} \\ \frac{\partial u_{main}}{\partial \omega_{main}} & \frac{\partial u_{main}}{\partial \varphi_{main}} & \frac{\partial u_{main}}{\partial \kappa_{main}} & \frac{\partial u_{main}}{\partial t_{xmain}} & \frac{\partial u_{main}}{\partial t_{ymain}} & \frac{\partial u_{main}}{\partial t_{zmain}} \end{bmatrix} \\ N_{main} = \begin{bmatrix} \frac{\partial u_{main}}{\partial X} & \frac{\partial u_{main}}{\partial Y} & \frac{\partial u_{main}}{\partial Z} \\ \frac{\partial u_{main}}{\partial X} & \frac{\partial u_{main}}{\partial Y} & \frac{\partial u_{main}}{\partial Z} \end{bmatrix} \\ \delta_{cmain} = [\Delta\omega_{main} \quad \Delta\varphi_{main} \quad \Delta\kappa_{main} \quad \Delta t_{xmain} \quad \Delta t_{ymain} \quad \Delta t_{zmain}] \\ \delta_{tmain} = [\Delta X \quad \Delta Y \quad \Delta Z] \\ L_{main} = \begin{bmatrix} u_{main} - \hat{u}_{main} \\ v_{main} - \hat{v}_{main} \end{bmatrix} \end{array} \right. \quad (5)$$

All the parameter information of the main camera can be obtained using Eq. (5). The binocular vision beam adjustment method makes full use of the rigidly fixed constraint relationship between the main camera and the assistant camera, and expresses the external parameters of the auxiliary camera with the external parameters of the main camera. By calibrating the binocular vision relative position parameters, the rigid fixed geometric constraint relationship $(R_{assistant}^{main}, T_{assistant}^{main})$ between the assistant camera and the main camera can be obtained. Then, the external parameters $(R_{assistant}, T_{assistant})$ of the assistant camera can be shown in Eq. (6).

$$\left\{ \begin{array}{l} R_{assistant} = R_{assistant}^{main} R_{main} \\ T_{assistant} = T_{assistant}^{main} + R_{assistant}^{main} T_{main} \end{array} \right. \quad (6)$$

According to Eq. (6), the imaging model of the assistant camera can be obtained, as shown in Eq. (7).

$$\lambda \begin{bmatrix} u_{assistant} \\ v_{assistant} \end{bmatrix} = K_{assistant} \begin{bmatrix} R_{assistant}^{main} R_{main} & T_{assistant}^{main} + R_{assistant}^{main} T_{main} \end{bmatrix} \begin{bmatrix} X \\ Y \\ Z \\ 1 \end{bmatrix} \quad (7)$$

Here, $(u_{assistant}, v_{assistant})$ represents the pixel coordinates of the image taken by the auxiliary camera and $K_{assistant}$ represents the internal parameter of the auxiliary camera.

According to Eq. (7), the external parameter corrections of the main and assistant cameras are the same as the 3D point coordinate corrections, so only the external parameter and 3D point corrections of the main camera need to be calculated in the optimization of the approach. In the optimization of the binocular vision beam adjustment algorithm, the parameters to be optimized are reduced, which will greatly reduce the running time and calculation amount of binocular vision.

3.3 Mathematical model of flatness

The flatness calculation method model is mainly introduced here. The IVMP primarily uses the least square method (LSM)^(18,19) and the particle swarm optimization (PSO) algorithm^(20–22) for flatness calculation. The IVMP collects the spatial coordinates of the antenna plane landmark points. An ideal plane is fitted with the detected coordinate data, and then the flatness of the antenna is calculated using the distance from the landmark point to the ideal plane.^(23,24) We assume that the direction vector of the antenna reference plane can be represented by (A, B, C) , and the reference plane Γ is composed of n landmark points. The equation of the antenna reference plane Γ is shown in Eq. (8).

$$Ax + By + Cz + D = 0 \quad (8)$$

The deviation d_i of each feature point $p_i(x_i, y_i, z_i)$ from the landmark point to the reference surface can be expressed as

$$d_i = \frac{Ax_i + By_i + Cz_i + D}{\sqrt{A^2 + B^2 + C^2}}. \quad (9)$$

The maximum distance $(d_i)_{max}$ and the minimum distance $(d_j)_{min}$ between the mark point and the reference surface can be obtained using Eq. (9). By defining the flatness error, the latter can be further written as

$$\Delta = (d_i)_{max} - (d_j)_{min}. \quad (10)$$

According to Eqs. (8) and (9), four parameter values A, B, C , and D need to be determined to calculate the reference surface Γ and the flatness error Δ . The commonly used method is the LSM.⁽²⁵⁾ In the evaluation of the flatness error Δ , we determine the direction of the reference plane Γ by continuously iterating the normal vector of the reference plane Γ . The normal vector direction A, B, C of the reference plane Γ is the most important parameter, and the specific position parameter D of the reference plane Γ has no effect on the evaluation of the flatness error.

In this paper, the PSO⁽²⁶⁾ is used to compute the flatness error Δ . In the particle swarm algorithm model, each particle's own state is described by a set of position and velocity vectors representing the feasible solution of the problem and its direction of motion in the search space.⁽²⁷⁾ The particle follows the global optimal search by continuously learning and comparing the group and neighbor optimal solutions. The particle velocity and position update equations are the core of the PSO algorithm and are described by

$$\varpi_{i,j}(t+1) = w\varpi_{i,j}(t) + c_1r_1(p_{best,i,j}(t) - x_{i,j}(t)) + c_2r_2(g_{best,i,j}(t) - x_{i,j}(t)). \quad (11)$$

Here, i is the index of the particle. j represents the dimension index of the particle. $\varpi_{i,j}(t)$ is the velocity of the i th particle at the t times iteration in j dimensional space. $x_{i,j}(t)$ represents the position of the i th particle in j dimensional space. p_{best} is the optimal value for particles, g_{best} is the global optimal value, t is the number of iterations, c_1 , c_2 represent an acceleration or learning factor, and r_1 , r_2 are random numbers in the interval $[0,1]$. The flatness error Δ is shown as

$$\min(\Delta) = \left((d_i)_{max} - (d_j)_{min} \right) = \min \left(\frac{A(x_i - x_j) + B(x_i - x_j) + C(x_i - x_j)}{\sqrt{A^2 + B^2 + C^2}} \right). \quad (12)$$

The differential evolution (DE) algorithm⁽²⁸⁾ is a random search algorithm for global optimization problems, which can meet the needs of fast and accurate detection of a large satellite antenna. A single DE algorithm has the problem of low convergence speed in the processing of a large amount of data, so the PSO algorithm integrated into the DE algorithm can make up for the limitations of this problem. The DE algorithm has three steps: mutation, crossover, and selection.

Mutation strategy: the mutation strategy of $rand / 1$ was used. In the t generation iteration, for each particle vector $x_i(t)$, a mutation vector, $\varpi_i(t)$, is generated by the mutation operator. Specifically, three particles, $x_\delta(t)$, $x_\rho(t)$, and $x_g(t)$, were randomly selected from the population, and $\delta = \rho = g$. The mutation vector calculation equation is

$$\varpi_i = x_\delta(t) + F \times (x_g(t) - x_\rho(t)). \quad (13)$$

Here, F is the variation scale factor, which is used to scale the difference vector and control the search step size.

Crossover operation: the DE algorithm uses a discrete crossover operator. The mutation vector ϖ_i obtained by the crossover operator through mutation operation is discretely crossed with the particle vector $x_i(t)$ to generate the test vector $\alpha_{i,j}$. The specific cross operation is shown as

$$\alpha_{i,j} = \begin{cases} \varpi_{i,j}, & rand \leq Cg \text{ or } j = j_{rand} \\ x_{i,j}, & otherwise \end{cases}. \quad (14)$$

Here, C_g is the cross-probability factor and j_{rand} is a random number between 1 and D .

Selection operation: after the next-generation population is generated by mutation and crossover operations, the one-to-one greedy screening operator is used to compare the child particle with the corresponding parent particle, and the better one is saved to the next generation. The selection operation is shown as

$$x_i(t+1) = \begin{cases} \alpha_i(t), & f(\alpha_i) \leq f(\alpha_i(t)) \\ x_{i,j}, & \text{otherwise} \end{cases} \quad (15)$$

The convergence velocity of the DE algorithm is low and that of the PSO algorithm is high. The DE and PSO algorithms are combined into a new optimization algorithm. In the iterative process, particles update their own velocity and position, so as to quickly approach the optimal value and improve the convergence velocity of the DE algorithm.⁽²⁹⁾

After the mutation vector is generated by mutation operation in the DE algorithm, because the direction of the mutation vector is random, the directions of the particle and global optimal positions are dynamically adjusted, and the particle position is constantly updated and the global optimal value is approached quickly. In this way, the convergence speed of the DE algorithm can be effectively improved in each iteration, as shown in Fig. 10.

The PSO algorithm is introduced into the DE algorithm.⁽³⁰⁾ On the one hand, it improves the convergence speed; on the other hand, it improves the probability of convergence to the global optimal value and ensures the accuracy and stability of the detection results. This intelligent optimization algorithm has the advantages of fast convergence, high probability, and good robustness. Combined with the flatness error monitoring model, it can quickly process the flatness monitoring data of large-scale satellites and obtain accurate detection results. The specific operation process is shown in Fig. 11.

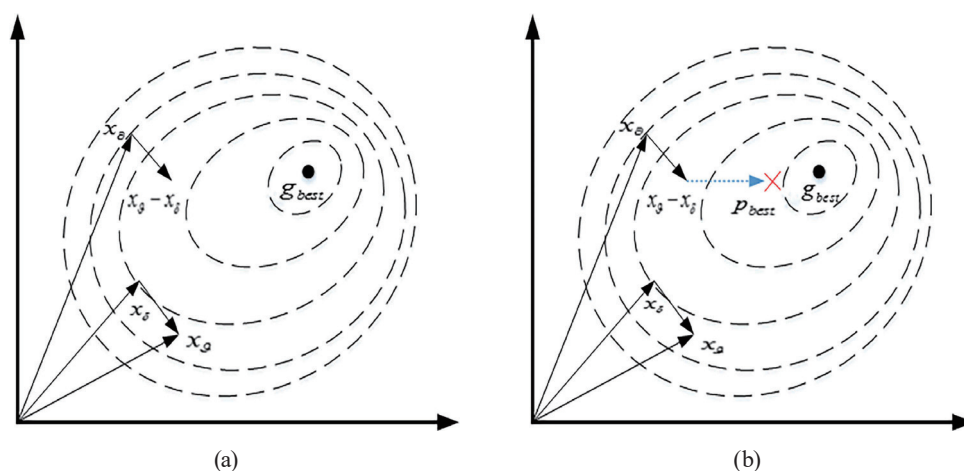


Fig. 10. (Color online) Mutation strategy diagram. (a) Variation operation. (b) Improved variation operation.

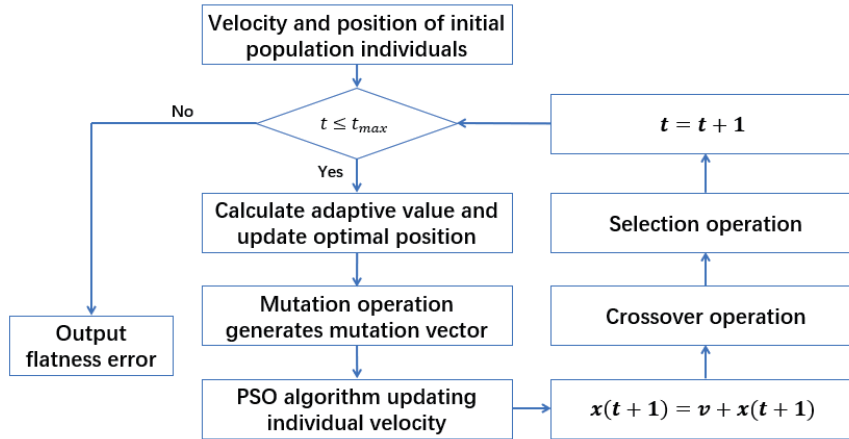


Fig. 11. (Color online) Solution process of flatness error.

Step 1. Set the initial parameters and position. In the search space, the position of A particles in the initial population is randomly selected using the DE algorithm. The initial positions of particles in the population are shown as

$$x = x_{min} + rand(E, D) \times (x_{min} - x_{min}). \quad (16)$$

Here, $x_{min} - x_{min}$ is the range of particle positions.

Step 2. Judge whether the cyclic condition $t \leq t_{max}$ is true, if so, execute step 3. Otherwise, calculate the optimal flatness error; t_{max} is the maximum number of iterations.

Step 3. Calculate the result value of all particles according to Eq. (12). The global optimal value g_{best} of the population is updated. The initial position of the particle is taken as the initial optimal value p_{best} .

Step 4. The $current-rand/1$ mutation strategy is used to mutate each particle. The DE algorithm is used to generate the mutation vector, as shown in Eq. (17).

$$x(t+1) = x_i(t) + F(x_g(t) - x_\delta(t)) \quad (17)$$

Here, $x_g(t)$, $x_\delta(t)$ is a random selection of two different particles in the t th iteration.

Step 5. Update the particle velocity according to the PSO equation Eq. (11). The updated velocity direction is added to the mutation operation to generate the next generation of particle vectors, as shown in Eq. (18).

$$x(t+1) = \omega_{i,j}(t+1) + x(t+1) \quad (18)$$

Step 6. According to Eqs. (14) and (15), the crossover and selection operations of the DE algorithm are carried out to update the optimal position of particles and then we return to step 2. Determine whether the convergence condition is satisfied.

4. Experimental Process

Experiments conducted to verify the robustness and reliability of the IVMP are discussed in this section. Two main experiments were carried out: (1) the repetitive detection of the three-dimensional coordinates of the markers on the antenna surface and (2) the antenna flatness repeatability test. The relative error analysis of the results of each test verifies the robustness and reliability of this method.

Firstly, the IVMP detects the same antenna plane three times. The size of the antenna is 2.5 m \times 10 m, and 2 datum rulers are placed; 191 landmark points are arranged on the antenna plane. The vertical distance between the IVMP and the antenna plane is 2.5 m. Forty-eight photos are collected each time. The results of the 3D coordinate repeatability test (three times in total) are shown in Figs. 12–14. The coordinate comparison results of three detection landmark points are shown in Fig. 15.

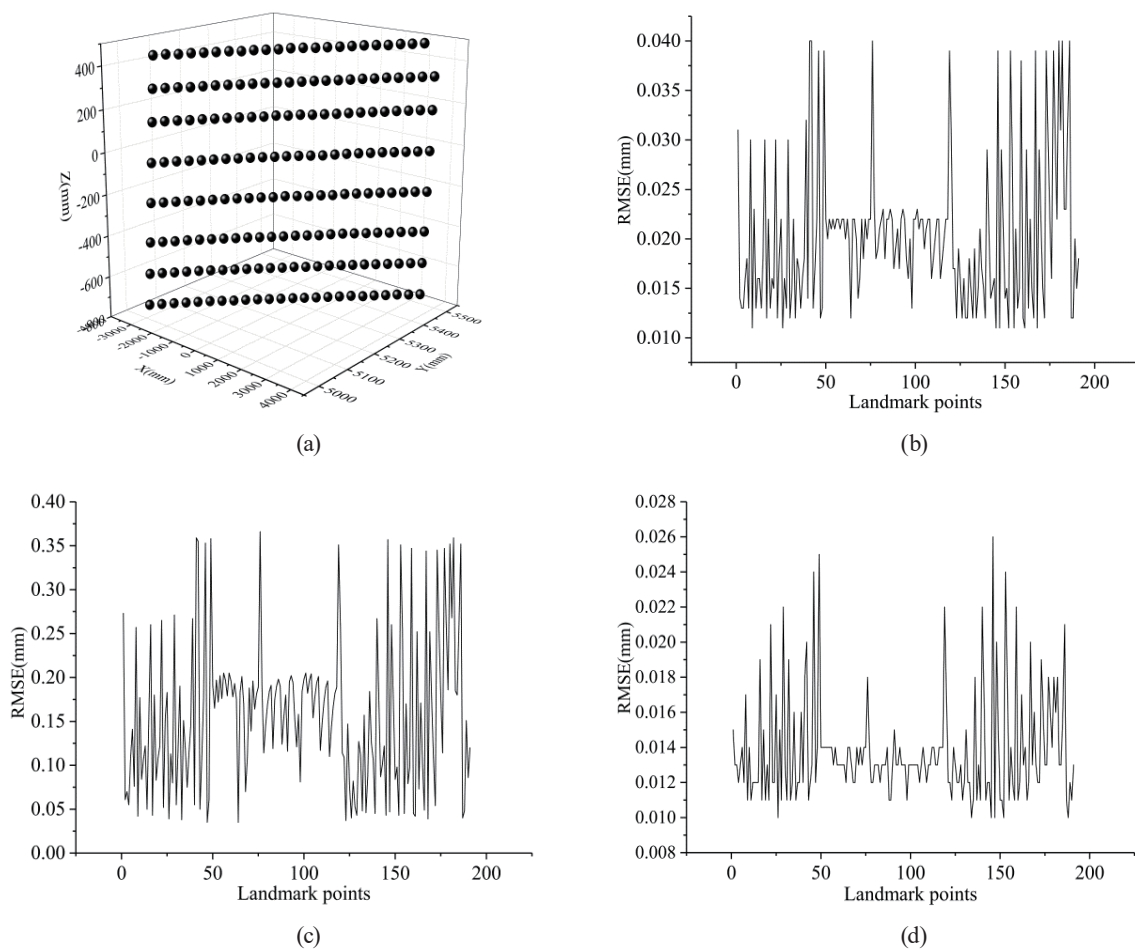


Fig. 12. First detection coordinate values and root mean square errors. (a) Spatial distribution of points. (b) X -axis root mean square error. (c) Y -axis root mean square error. (d) Z -axis root mean square error.

In Fig. 12, (a) is the lattice distribution of the coordinate values of the antenna plane in the three-dimensional space for the first detection of the IVMP; (b) is the root mean square error (RMSE) of the coordinate value on the X -axis and the maximum RMSE is 0.040 mm; (c) is the RMSE of the coordinate value on the Y -axis and the maximum RMSE is 0.366 mm; (d) is the RMSE of the coordinate value on the Z -axis and the maximum RMSE is 0.026 mm. The RMSE is obtained using Eq. (19); $x_{obs,i}$ denotes the observed value and $x_{model,i}$ denotes the true value.

$$RMSE = \sqrt{\frac{\sum_{i=1}^n (x_{obs,i} - x_{model,i})^2}{n}} \quad (19)$$

In Fig. 13, (a) is the lattice distribution of the coordinate values of the antenna plane in the three-dimensional space for the second detection of the IVMP; (b) is the RMSE of the coordinate value on the X -axis and the maximum RMSE is 0.021 mm; (c) is the RMSE of the coordinate

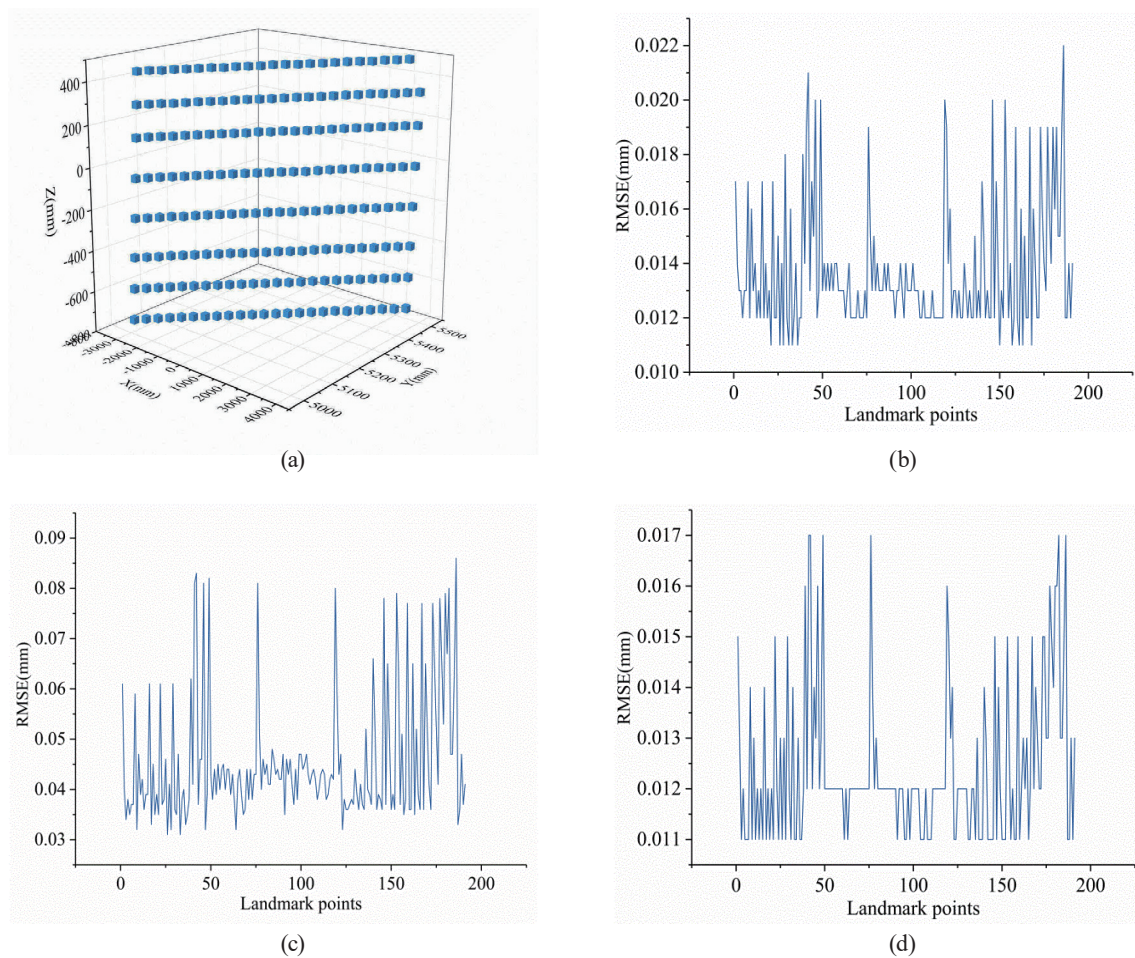


Fig. 13. (Color online) Second detection coordinate values and root mean square errors. (a) Spatial distribution of points. (b) X -axis root mean square error. (c) Y -axis root mean square error. (d) Z -axis root mean square error.

value on the Y -axis and the maximum RMSE is 0.083 mm; (d) is the RMSE of the coordinate value on the Z -axis and the maximum RMSE is 0.017 mm.

In Fig. 14, (a) is the lattice distribution of the coordinate values of the antenna plane in the three-dimensional space for the third detection of the IVMP; (b) is the RMSE of the coordinate value on the X -axis and the maximum RMSE is 0.037 mm; (c) is the RMSE of the coordinate value on the Y -axis and the maximum RMSE is 0.225 mm; (d) is the RMSE of the coordinate value on the Z -axis and the maximum RMSE is 0.023 mm.

In Figs. 12–14, the IVMP continuously detects the coordinate data of the antenna surface and the RMSE of each axis in the same environment three times. It can be seen from the figure that the distribution trend of the RMSE of each axis is basically the same. The maximum RMSEs of the three-times-detected coordinates of the landmark point are 0.04 mm on the X -axis and 0.366 mm on the Y -axis. The maximum RMSE on the Z -axis is 0.026 mm.

In Fig. 15, the coordinate comparison of the three-time-detected coordinate values of the IVMP is shown in the same space. It can be seen from Fig. 16 that the coordinates of the three detection points coincide. The IVMP detects thrice the coordinate data of the antenna surface and the RMSE of each axis continuously.

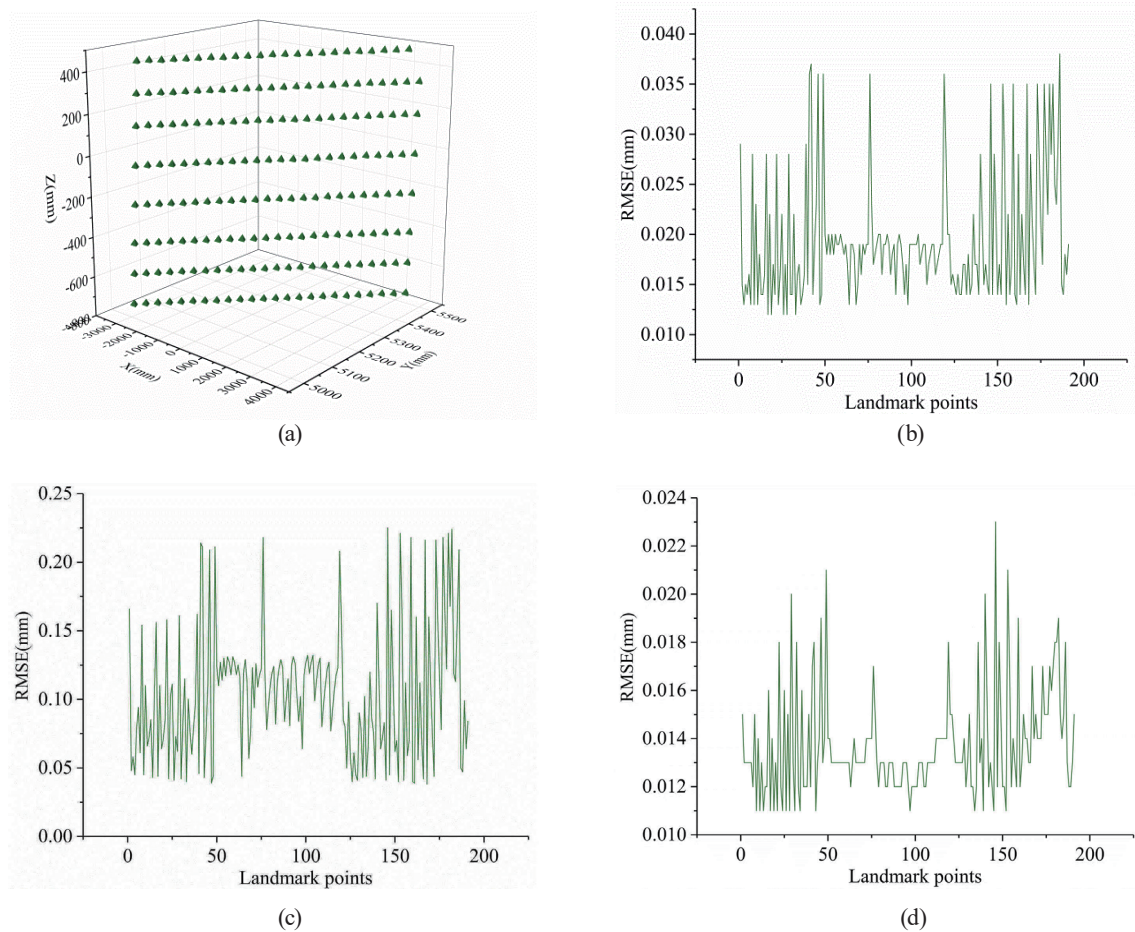


Fig. 14. (Color online) Third detection coordinate values and root mean square errors. (a) Spatial distribution of points. (b) X -axis root mean square error. (c) Y -axis root mean square error. (d) Z -axis root mean square error.

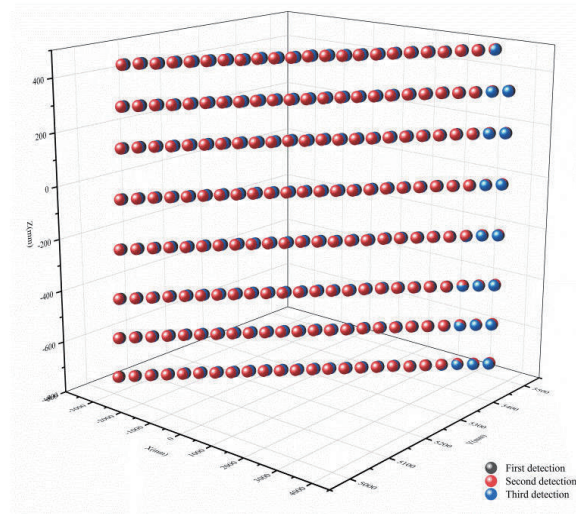


Fig. 15. (Color online) Comparison of three-time-detected coordinate values.



Fig. 16. (Color online) Laser tracking and theodolite systems. (a) API tracker 3 laser tracking system. (b) Leica theodolite system.

It can be obtained from Figs. 12–15 that the coordinate values of the antenna surface detected three consecutive times by the IVMP are basically the same, which meets the accuracy requirements of flatness detection. The RMSE distribution trend is basically the same. The robustness and integrity of the IVMP are verified.

Secondly, we test the repeatability of the antenna flatness. According to the flatness calculation model, the coordinate values detected three consecutive times by the IVMP are calculated for flatness. The three-time flatness test results are obtained, as shown in Table 2. The results of three-time flatness detection are analyzed.

It can be seen from Table 2 that the flatness detected three times by the IVMP is basically the same, and the repeatability of the flatness detection is better than 0.01 mm. The maximum deviation of three inspections is 1.103 mm. The minimum deviation is -1.157 mm. The difference

Table 2
Flatness detection repetition.

Detection	Flatness (mm)	Largest deviation (mm)	Smallest deviation (mm)	Deviation range (mm)
Scenario 1	0.326	1.115	-1.127	2.242
Scenario 2	0.328	1.126	-1.121	2.247
Scenario 3	0.324	1.103	-1.136	2.239

in maximum deviation is less than 0.03 mm. The difference in minimum deviation is less than 0.02 mm. The difference in the deviation range should be less than 0.01 mm.

5. Results and Discussion

The performance of the IVMP in terms of precision and efficiency comparisons is discussed as follows.⁽¹⁾ The flatness of the IVMP is compared with those of the laser tracking and theodolite systems.⁽²⁾ The speed (efficiency) of the IVMP is compared with those of laser scanners, the laser tracking system, and the theodolite system. Through the comparative analysis of the two aspects, it can be explained that the IVMP meets the accuracy requirements of flatness detection and has the advantages of independent rapid detection.

The accuracy of the IVMP is analyzed. Firstly, the IVMP collects the coordinates of the antenna surface at fixed points and calculates the antenna flatness. The flatness of the antenna surface is then measured using the laser tracking and theodolite systems (Fig. 16). Finally, the flatness of the IVMP is compared with those of the laser tracking and theodolite systems. The comparison results are shown in Tables 3 and 4. The deviation comparison results are shown in Figs. 17 and 18.

It can be seen from Table 3 and Fig. 17 that the difference between the flatness detected by the IVMP and the flatness detected by the API tracker 3 is less than 5×10^{-2} mm. The maximum deviation is less than 2×10^{-2} mm. The minimum deviation is less than 2×10^{-2} mm. Given the high detection accuracy and reliability of the API tracker 3, the accuracy and reliability of the intelligent vision platform are verified.

It can be seen from Table 4 and Fig. 18 that the flatness difference between the IVMP and the theodolite system is less than 10^{-1} mm. The difference in maximum deviation is less than 10^{-2}

Table 3
Flatness detection compared with API tracker 3.

Detection	Flatness (mm)	Largest deviation (mm)	Smallest deviation (mm)	Deviation range (mm)
IVMP	0.860	0.388	-0.472	0.5
API Tracker 3	0.903	0.406	-0.497	0.5

Table 4
Flatness detection compared with theodolite.

Detection	Flatness (mm)	Largest deviation (mm)	Smallest deviation (mm)	Deviation range (mm)
IVMP	0.860	0.388	-0.472	0.5
Theodolite	0.789	0.394	-0.395	0.4

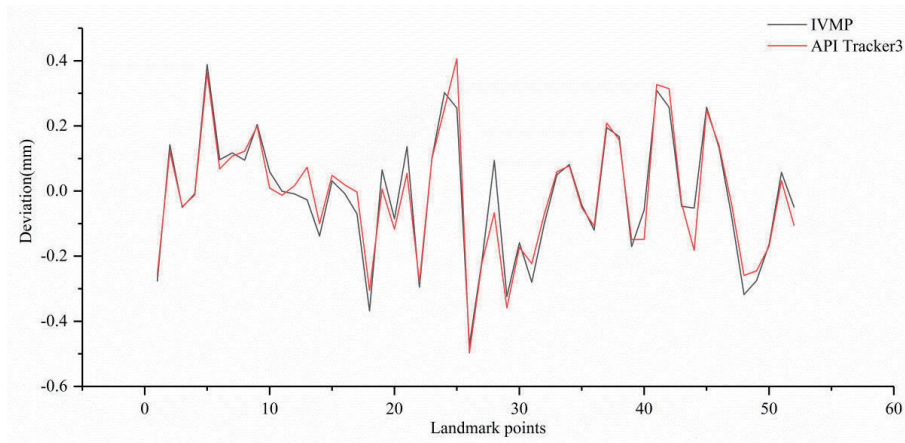


Fig. 17. (Color online) Deviation compared with API tracker 3.

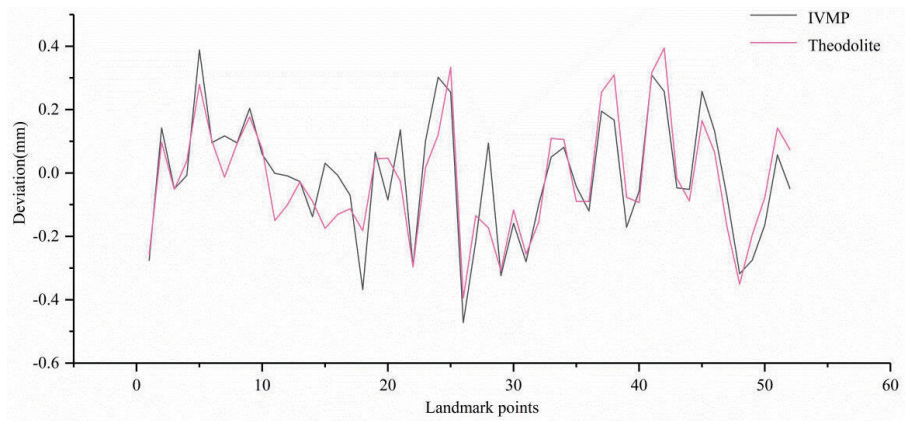


Fig. 18. (Color online) Deviation compared with theodolite.

mm. The difference in minimum deviation is less than 10^{-1} mm. The maximum difference is less than 10^{-1} mm. The API tracker 3 is used to obtain the true value. By comparison, the precision of intelligent vision platforms is 10% higher than that of the theodolite system.

The detection efficiency of the IVMP is analyzed. The detection time of the IVMP is compared with those of the laser scanner, API tracker 3, and theodolite system. With the same antenna and feature points (50, 100, 150) in the same environment, the antenna surface coordinate value acquisition and flatness detection are completed by using the IVMP, laser scanner, API tracker 3, and theodolite system in their respective running periods. At the beginning of detection, the effective detection times of the four methods were recorded and compared. The comparison results of detection times of the four methods are shown in Table 5.

It can be seen from Table 5 that the detection efficiency of the IVMP is inferior to that of laser scanners when the number of feature points is the same. Compared with the API tracker 3 and the theodolite system, the detection speed of the IVMP is improved by 48 and 60.6%, respectively. Owing to the well-established measurement system and high precision at the expense of time, the IVMP is better than the API tracker 3 and the theodolite system, and it is

Table 5
Comparison of detection time.

Number of feature points	IVMP (h)	Laser Scanner (h)	API Tracker 3 (h)	Theodolite (h)
Time (50)	0.13	0.10	0.25	0.33
Time (100)	0.13	0.10	0.52	0.69
Time (150)	0.13	0.10	0.79	1.03

worse than the laser scanner. With the increases in the detection range and the number of target points, the detection time gap between the IVMP and the API tracker 3 and the theodolite system will become increasingly larger, which shows the advantage of the IVMP in the rapid detection of targets.

5. Conclusions

In this paper, we propose a set of IVMP detection methods to challenge the problems in large-scale target detection, such as in antenna flatness detection. It can quickly, accurately, and automatically acquire target information and realize mobile in-position, discontinuous surface, and large-size autonomous rapid detections.

Through flatness measurement and efficiency comparison, the accuracy and reliability of the IVMP can meet the quality inspection requirements of satellite antennas. With the increases in the detection range and number of marker points, the superiority of the IVMP for rapid detection is increasingly demonstrated.

Acknowledgments

The authors wish to acknowledge the support of the National Natural Science Foundation of China (No. 61902016), Natural Science Foundation of Beijing Municipality (No. 4204093), and National Key R&D Program of China (No. 2018YFC0807806-2).

References

- 1 G. Maculotti, X. Feng, R. Su, M. Glaetto, and R. Leach: *Meas. Sci. Technol.* **30** (2019) 075005. <https://doi.org/10.1088/1361-6501/ab188f>
- 2 G. Moona, R. Sharma, U. Kiran, and K. P. Chaudhary: *MAPAN* **29** (2014) 261. <https://doi.org/10.1007/s12647-014-0106-0>
- 3 P. Křen: *Meas. Sci. Technol.* **25** (2014) 044017. <https://doi.org/10.1088/0957-0233/25/4/044017>
- 4 H. Liu, Z. Dong, H. Huang, R. Kang, and P. Zhou: *Meas. Sci. Technol.* **26** (2015) 115008. <https://doi.org/10.1088/0957-0233/26/11/115008>
- 5 J. Li, J. Yang, S. Wu, and X. Cao: *Int. J. Optomechatron.* **12** (2018) 53. <https://doi.org/10.1080/15599612.2018.1529846>
- 6 W. Zhu, X. Cao, T. Fan, S. Wu, J. Li, and J. Yang: 9th Int. Symp. Precision Engineering Measurement and Instrumentation. International Society for Optics and Photonics **9446** (2015) 94461I. <https://doi.org/10.1117/12.2180817>
- 7 Q. Li: *IEEE Sens. J.* **13** (2013) 2051. <https://doi.org/10.1109/JSEN.2013.2249511>
- 8 M. Chen, S. Takahashi, and K. Takamasu: *Int. J. Precis. Eng. Manuf.* **17** (2016) 1093. <https://doi.org/10.1007/s12541-016-0133-6>
- 9 I. Fujimoto, K. Nishimura, T. Takatsuji, and Y. Pyun: *Precis. Eng.* **36** (2012) 270. <https://doi.org/10.1016/j.precisioneng.2011.11.001>

- 10 I. Fujimoto, T. Takatsuji, K. Nishimura, and Y. Pyun: Meas. Sci. Technol. **23** (2012) 115102. <https://doi.org/10.1088/0957-0233/23/11/115102>
- 11 J. Li, J. Yang, S. Wu, and X. Cao: Int. J. Optomechatron. **12** (2018) 53. <https://doi.org/10.1080/15599612.2018.1529846>
- 12 B. Wu and B. Wang: Adv. Mech. Eng. **5** (2013) 629385. <https://doi.org/10.1155/2013/629385>
- 13 Y. Yang, S. Song, F. Yue, W. He, W. Shao, K. Zhao, and W. Nie: Eng. Geol. **259** (2019) 105166. <https://doi.org/10.1016/j.enggeo.2019.105166>
- 14 X. Yang, S. Fang, B. Kong, and Y. Li: Optik **125** (2014) 3727. <https://doi.org/10.1016/j.ijleo.2014.03.009>
- 15 R. Chen, K. Zhong, Z. Li, M. Liu, and G. Zhan: Int. Soc. Opt. Photon. **10023** (2016) 1002319. <https://doi.org/10.1117/12.2245590>
- 16 R. Chen, K. Zhong, Z. Li, M. Liu, and G. Zhan: Int. Soc. Opt. Photon. **9276** (2014) 92761H. <https://doi.org/10.1117/12.2070957>
- 17 C. Xiao, L. Han, and S. Chen: Symmetry **13** (2021) 1195. <https://doi.org/10.3390/sym13071195>
- 18 H. Guo, P. Feng, and T. Tao: Opt. Lasers Eng. **48** (2010) 166. <https://doi.org/10.1016/j.optlaseng.2009.04.005>
- 19 K. R. Naqvi: J. Phys. Chem. Lett. **7** (2016) 676. <https://doi.org/10.1109/TPEL.2010.2100101>
- 20 K. Ishaque, Z. Salam, M. Amjad, and S. Mekhilef: IEEE Trans. Power Electron. **27** (2012) 3627. <https://doi.org/10.1109/TPEL.2012.2185713>
- 21 K. Ishaque and Z. Salam: IEEE Trans. Power Electron. **60** (2012) 3195. <https://doi.org/10.1109/TIE.2012.2200223>
- 22 M. A. Hassan and M. A. Abido: IEEE Trans. Power Electron. **26** (2010) 755. <https://doi.org/10.1109/TPEL.2010.2100101>
- 23 L. Yin and Z. Wang: Results Phys. **15** (2019) 102594. <https://doi.org/10.1016/j.rinp.2019.102594>
- 24 Z. Wang: Opt. Express. **23** (2015) 1912. <https://doi.org/10.1364/OE.23.001912>
- 25 P. Bringmann, C. Carstensen, and G. Starke: SLAM J. Numer. Anal. **56** (2018) 428. <https://doi.org/10.1137/16M1083797>
- 26 A. Ratnaweera, S. K. Halgamuge, and H. C. Watson: IEEE Trans. Evol. Comput. **8** (2004) 240. <https://doi.org/10.1109/TEVC.2004.826071>
- 27 M. Zhang, Y. Liu, C. Sun, X. Wang, and J. Tan: Meas. Sci. Technol. **31** (2020) 085006. <https://doi.org/10.1088/1361-6501/ab8170>
- 28 Y. Wang, Z. Cai, and Q. Zhang: IEEE Trans. Evol. Comput. **15** (2011) 55. <https://doi.org/10.1109/TEVC.2010.2087271>
- 29 G. Wu, R. Mallipeddi, P. N. Suganthan, R. Wang, and H. Chen: Inf. Sci. **329** (2016) 329. <https://doi.org/10.1016/j.ins.2015.09.009>
- 30 J. Feng, J. Zhang, C. Wang, R. Jiang, and M. Xu: IEEE Access **8** (2020) 73204. <https://doi.org/10.1109/ACCESS.2020.2988530>

About the Authors



Dongwei Qiu is a civil engineer and geomatics researcher who earned his Ph.D. degree from Beijing Jiaotong University, China. In 2005, he began working at Beijing University of Civil Engineering and Architecture, China, where he is an associate professor at present. From 2019 to 2021, he was a visiting research professor at Drexel University, USA. His main research interests are in structural health monitoring, vision measurement, and sensor system. (qiudw@bucea.edu.cn)



Mingjian Xiao received his B.S. degree in engineering surveying from Beijing University of Civil Engineering and Architecture, China, in 2019. He is now studying for his M.S. degree in Beijing University of Civil Engineering and Architecture. His research interests include structural health monitoring and infrared thermography. (xmj@stu.bucea.edu.cn)



Shanshan Wan received her Ph.D. degree from the School of Computer Science & Technology, Beijing Institute of Technology, Beijing, China, in 2018. She is currently an associate professor with the Department of Computer Science, Beijing University of Civil Engineering and Architecture, China. Her current research interests include data mining, intelligent tutoring systems, intelligent building, and artificial intelligence. (wss@bucea.edu.cn)



Xingyu Wang received his B.S. degree from Beijing University of Civil Engineering and Architecture, China, in 2021. He is currently a graduate student at Beijing University of Civil Engineering and Architecture. His research interests include multiocular vision measurement and image processing. (k1941172018@163.com)

